Hydrodynamic benefits of intermittent locomotion of a self-propelled flapping plate

Kui Liu, Haibo Huang ⬤,[*] and Xi-Yun Lu

Department of Modern Mechanics, University of Science and Technology of China, Hefei 230026, China

Intermittent locomotion is a widely used behavioral strategy for fish and birds to reduce the cost of movement. The intermittent locomotion performance of a self-propelled flapping plate is investigated numerically. Two intermittent swimming modes, namely, the multiple-tail-beat mode (MT mode) and the half-tail-beat mode (HT mode), as well as the continuous swimming mode (CT mode), are considered. Performance is evaluated from propulsive speed, efficiency, and cost of transport. The hydrodynamic performances of the intermittent modes are found to be better than the hydrodynamic performance of the CT mode when the bending stiffness K is moderate [i.e., $K \approx O(1)$] and the duty cycle is not too small. For the two intermittent modes, the performance of the HT mode is better than that of the MT mode when K is small or moderate, while the situation is opposite when K is large. It is found that compared to the asymmetric wake of the MT mode, the symmetric wake of the HT mode is favorable to generate more thrust force and therefore achieve better performance. Besides, at moderate K, the largest bending deformation of the plate in the HT mode, as well as the large normal force, produces the largest thrust during the flapping. The present results can help us to better understand the intermittent locomotion of animals and may be helpful for bionic design.

I. INTRODUCTION

Intermittent locomotion is a widely adopted strategy for animals to save energy, especially when they are in long-distance migration. Birds use interspersed periods of flapping and gliding to reduce the mechanical requirements of level flight while undergoing cyclical changes in flight altitude, which is known as undulating flight [1–3]. Similarly to birds, lots of fish and marine animals swim in a special way where the whole cycle consists of an active burst phase and a passive coast phase, known as burst-and-coast swimming or intermittent swimming [1,4,5], which is quite different from the continuous swimming.

Evidence has shown that hydrodynamic benefits generate from the intermittent swimming style. Dynamical models proposed by Weihs [6,7] predicted that, to swim a given distance, more than 50% energy will be saved by adopting the intermittent swimming gait. Besides, compared with continuous swimming at the same mean speed, the burst-and-coast swimming style could save 14% to 19% energy [6]. Based on the Bone-Lighthill boundary layer thinning hypothesis, the above predictions showed that skin friction drag on a fish body may increase when it undulates [8]. Under the circumstances, a fish may then reduce its overall skin friction drag by interspersing an undulation phase with a coasting phase [9].

In experiments and observations, many results also have shown the superiority of an intermittent swimming gait. Ribak *et al.* [10] analyzed the swimming gait of cormorants, which swam underwater at shallow depth in a controlled research setup, by using kinematic analysis of video sequences. They estimated the resultant drag of the birds during the entire paddling cycle and concluded that the burst-and-glide gait may be beneficial even at lower speeds as the birds dive deeper. Wu *et al.* [11] observed the differences between two burst-and-coast modes, namely, the multiple-tail-beat mode (MT mode) and the half-tail-beat mode (HT mode) by quantifying the swimming kinematics and the flow patterns generated by the carps. Besides, it is estimated from digital particle image velocimetry experiments that the energy saving may be 45% when burst-and-coast swimming is adopted by the koi carps compared with steady or continuous swimming at the same mean speed. Gleiss *et al.* [1] experimented on four marine vertebrate species of sharks and pinnipeds and found that gait patterns resemble undulating flight. A direct comparison of continuous and intermittent swimming seals indicated that, during intermittent swimming, less locomotory effort was expended than during continuous swimming at corresponding velocities [1].

The experimental studies of living fish play an important role in deepening our understanding of the mechanics and mechanisms of the locomotion of fishes and birds. However, to control the movement of animals is very hard. Some important physical quantities, such as force and torque, are very difficult to measure. Besides, it may be difficult to figure out the effect of each control parameter on performance by operating corresponding experiments independently [12]. One way to overcome these difficulties is to replace live fish with mechanical devices or fish robotics in the research of fish locomotion [13]. Another efficient way is numerical simulation, which is extremely convenient to obtain critical information and details about the body and the flow field, such as power and vorticity. Results of two-dimensional numerical simulation by Chung [14] showed that intermittent swimming can save 56% energy compared with continuous swimming, which is comparable to the experimental result of Wu *et al.* [11]. Recently, through a simulation of the inviscid flow of a self-propelled swimmer, which consists of a virtual
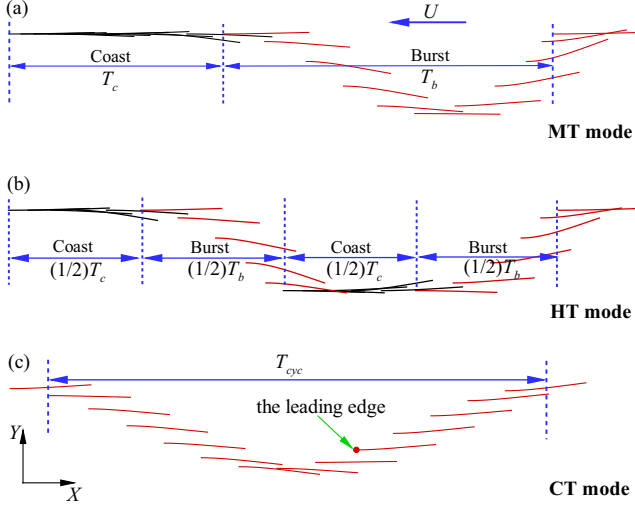
_____
*huanghb@ustc.edu.cn

FIG. 1. Schematic diagram of the locations and shapes of a flexible plate during one cycle period ($T_{\mathrm{cyc}} = T_c + T_b$) in the (a) MT, (b) HT, and (c) CT modes. The head of the plate is forced to heave up and down (the forcing is stopped during the coast period T_c). Due to the interaction of the plate and the surrounding fluid, the plate may deform passively and move forward (from right to left). T_b is the burst period, which is a constant in our study.

body and a two-dimensional hydrofoil pitching intermittently about its leading edge, Akoz and Moored [9] discovered an additional inviscid Garrick mechanism that can save intermittent swimmers as much as 60% of the energy. Dai *et al.* [12] numerically studied the intermittent locomotion performance of a fishlike elastic swimmer whose mass ratio and bending rigidity vary along the body. Their results indicated that, when the cruising Reynolds number (Re) was large enough and the duty cycle (DC) was moderate, the intermittent style was more economical than the continuous style, where DC is the ratio of the burst period (T_b) to the total cycle period (T_{cyc}), i.e., DC = T_b/T_{cyc}. Numerical simulation of a self-propelled plate at low Re (Re = 100) also showed some kind of superiorities of intermittent locomotion [15], because the maximum average cruising speed and the maximum swimming efficiency arises at DC = 0.9 and 0.3, respectively. However, it is ambiguous whether intermittent swimming is more energy efficient than continuous swimming because there is no direct comparison between them in the literature.

In the present study, the locomotion of a self-propelled flexible plate is systematically studied through numerical simulations. We consider three different swimming modes including the continuous mode (CT mode) and two intermittent modes, i.e., the MT and HT modes. We investigated the propulsion performance of the plate with the change of bending stiffness and the duty cycle. Our aim is to find out which mode is the optimal one and explore the inherent mechanisms.

II. PHYSICAL PROBLEM AND MATHEMATICAL FORMULATION

The schematic diagrams of the locations and shapes of a plate within one period for the three swimming modes are shown in Fig. 1. The leading edge of the plate is forced

to heave intermittently [Figs. 1(a) and 1(b)] or continuously [Fig. 1(c)] in the lateral direction. In each mode, the plates are in chronological order from right to left.

For the intermittent modes [the MT mode in Fig. 1(a) and the HT mode in Fig. 1(b)], $T_b = 1/f_0$ is the burst period, where f_0 is the base frequency, which is a constant. Hence, T_b is also a constant in our study. The total cycle period T_{cyc} is composed of burst and coast periods, i.e., $T_{\mathrm{cyc}} = T_b + T_c$, where T_c is the coast period.

An important adjustable parameter in the intermittent modes, the DC is introduced. It is a period ratio between the burst period and the total cycle, i.e,

$$\mathrm{DC} = \frac{T_b}{T_{\mathrm{cyc}}}. \qquad (1)$$

Since the burst period is less or equal to the total cycle, we have DC $\leqslant 1$. Through adjusting the DC, T_{cyc} and T_c are changeable. We have $T_{\mathrm{cyc}} = \frac{T_b}{\mathrm{DC}}$ and $T_c = T_b(\frac{1}{\mathrm{DC}} - 1)$. If DC = 1, it is a continuous flapping with $T_{\mathrm{cyc}} = T_b$ and $T_c = 0$.

For the MT mode [Fig. 1(a)], the heaving motion of the leading edge is prescribed by

$$y(t) = \begin{cases} A\cos(2\pi f_0 t), & 0 \leqslant t \leqslant T_b, \\ A, & T_b \leqslant t \leqslant T_{\mathrm{cyc}}, \end{cases} \qquad (2)$$

For the HT mode [Fig. 1(b)], the heaving motion of the leading edge is prescribed by

$$y(t) = \begin{cases} A\cos(2\pi f_0 t), & 0 \leqslant t \leqslant \frac{T_b}{2}, \\ -A, & \frac{T_b}{2} \leqslant t \leqslant \frac{T_{\mathrm{cyc}}}{2}, \\ A\cos\{2\pi f_0[t - (T_{\mathrm{cyc}} - T_b)/2]\}, & \frac{T_{\mathrm{cyc}}}{2} \leqslant t \leqslant \frac{T_{\mathrm{cyc}}}{2} + \frac{T_b}{2}, \\ A, & \frac{T_{\mathrm{cyc}}}{2} + \frac{T_b}{2} \leqslant t \leqslant T_{\mathrm{cyc}}. \end{cases} \qquad (3)$$

For the CT mode [Fig. 1(c)], the forced motion of the leading edge is

$$y(t) = A\cos(2\pi f_c t), \qquad (4)$$

where A is the amplitude and f_c is the heaving frequency. Here an adjustable frequency ratio for the CT mode, $f_r = f_c/f_0$, is introduced. Equation (4) can be written as

$$y(t) = A\cos(2\pi f_r f_0 t). \qquad (5)$$

It is noticed that $f_r \leqslant 1$ in our study of the CT mode. The total cycle period $T_{\mathrm{cyc}} = T_b/f_r$ is larger or equal to T_b, which is a constant. In the continuous mode, $f_0 = \frac{1}{T_b}$ is the largest flapping frequency in our simulations. Due to the largest energy input of the fastest flapping, it may achieve the highest cruising speed. The plate may decrease its frequency ($f_r < 1$) to achieve a lower cruising speed.

In these actuation modes, only the leading edge of the plate is restricted with the prescribed lateral heaving motion. There is no active pitching. Due to fluid-structure interaction, the plate may deform and pitch passively, which results in horizontal locomotion. The heaving flexible plate has been used to model the general self-propulsive swimming [16–19] because it not only includes the active heaving motion but also includes the passive pitching motion. Despite its limitations of the simple actuation, we feel that the results obtained from

this model may incorporate enough physics to contribute to a better understanding of the problem.

To simulate the fluid flow, the incompressible Navier-Stokes equations are adopted:

$$\frac{\partial \boldsymbol{v}}{\partial t} + \boldsymbol{v} \cdot \nabla \boldsymbol{v} = -\frac{1}{\rho}\nabla p + \frac{\mu}{\rho}\nabla^2 \boldsymbol{v} + \boldsymbol{f}_b, \qquad (6)$$

$$\nabla \cdot \boldsymbol{v} = 0, \qquad (7)$$

where $\boldsymbol{v}$ is the velocity, p is the pressure, ρ is the density of the fluid, μ is the dynamic viscosity, and $\boldsymbol{f}_b$ is the Eulerian momentum force acting on the surrounding fluid due to the immersed boundary, as constrained by the no-slip boundary condition.

The structural equation is employed to describe the deformation and motion of the plate [20,21],

$$\rho_l \frac{\partial^2 \boldsymbol{X}}{\partial t^2} - \frac{\partial}{\partial s}\left[Eh\left(1 - \left|\frac{\partial \boldsymbol{X}}{\partial s}\right|^{-1}\right)\frac{\partial \boldsymbol{X}}{\partial s}\right] + EI\frac{\partial^4 \boldsymbol{X}}{\partial^4 s} = F_s, \quad (8)$$

where s is the Lagrangian coordinate along the plate, ρ_l is the structural linear mass density, $\boldsymbol{X}(s,t) = [X(s,t), Y(s,t)]$ is the position vector of the plate, and F_s is the Lagrangian force exerted on the plate by the surrounding fluid. E is the Young's modulus of the plate, h is the thickness of the plate, and I is the moment of inertia of the plate section. Eh and EI denote the structural stretching rigidity and bending rigidity, respectively. At the leading edge of the plate, the clamped boundary condition is adopted, i.e.,

$$-Eh\left(1 - \left|\frac{\partial \boldsymbol{X}}{\partial s}\right|^{-1}\right)\frac{\partial \boldsymbol{X}}{\partial s} + EI\frac{\partial^3 \boldsymbol{X}}{\partial^3 s} = 0,$$

$$Y(t) = y(t), \qquad \frac{\partial \boldsymbol{X}}{\partial s} = (1, 0). \qquad (9)$$

At the free end of the plate, the boundary conditions are expressed as

$$-Eh\left(1 - \left|\frac{\partial \boldsymbol{X}}{\partial s}\right|^{-1}\right)\frac{\partial \boldsymbol{X}}{\partial s} + EI\frac{\partial^3 \boldsymbol{X}}{\partial^3 s} = 0, \qquad \frac{\partial^2 \boldsymbol{X}}{\partial s^2} = 0. \quad (10)$$

In addition, $\boldsymbol{X}(s, 0) = [s, y(0)]$ and $\partial \boldsymbol{X}/\partial t(s, 0) = (0, 0)$ are the initial conditions for the plate.

To normalize the above equations, the characteristic quantities ρ, L, and U_{ref} are chosen where ρ is the fluid density, L is the dimensional length of the plate, and U_{ref} is the maximum flapping velocity of the leading edge in the lateral direction, i.e., $U_{\mathrm{ref}} = 2\pi A f_0$. Therefore, the characteristic time is $T_{\mathrm{ref}} = L/U_{\mathrm{ref}}$. Based on dimensionless analysis, the following dimensionless governing parameters are introduced: the duty cycle DC, the frequency ratio f_r, the Reynolds number $\mathrm{Re} = \rho U_{\mathrm{ref}} L/\mu$, the heaving amplitude A, the mass ratio of the plate to the fluid $M = \rho_l/\rho L$, the stretching stiffness $S = Eh/\rho U_{\mathrm{ref}}^2 L$, and the bending stiffness $K = EI/\rho U_{\mathrm{ref}}^2 L^3$.

III. NUMERICAL METHOD AND VALIDATION

The governing equations of the fluid-plate problem are solved numerically by an immersed boundary-lattice Boltzmann method for the fluid flow and a finite element method for the motion of the flexible plate. The immersed boundary method has been widely applied to problems relating to moving boundaries immersed in a viscous fluid
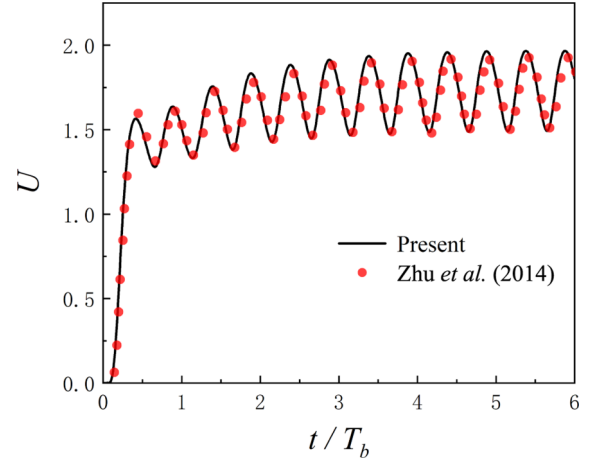

FIG. 2. Validation for the case of a self-propelled plate flapping continuously with the nondimensional governing parameters: $\mathrm{Re} = 200$, $A = 0.5$, $M = 0.2$, $K = 0.8$, and $S = 1000$ (Zhu *et al.* [16]). The streamwise velocity of the leading edge as a function of time is presented.

flow [22,23], while the lattice Boltzmann method has been extensively used to simulate complex flows as an alternative to conventional numerical methods for the Navier-Stokes equations [19,24–27]. Here we combine these two methods to solve the fluid-structure problem. The body force term $\boldsymbol{f}_b$ in Eq. (6) represents an interaction force between the fluid and the immersed boundary to enforce the no-slip velocity boundary condition. Equation (8) for the plate is discretized by a finite element method, and deformations with a large displacement of the plate are handled by the corotational scheme [28]. More details on numerical methods can be found in our previous papers (Tian *et al.* [29], Hua *et al.* [21], Huang *et al.* [30]).

To validate the numerical method, a single plate in isolated swimming [16] was simulated with $\mathrm{Re} = 200$, $A = 0.5$, $M = 0.2$, $K = 0.8$, and $S = 1000$. In the simulation, the computational domain for fluid flow is chosen as $[-15, 25] \times [-15, 15]$ in the x and y directions, which is sufficiently large so that the blocking effects of the boundaries are not significant. A constant pressure with $\boldsymbol{v} = 0$ is imposed at all boundaries except for the outlet where $\partial \boldsymbol{v}/\partial x = 0$ with constant pressure is imposed [31]. Initially, the fluid velocity field is zero in the entire computational domain. In the x and y directions the mesh is uniform with spacing $\Delta x = \Delta y = 0.01L$, where L is the dimensional length of the plate. The time step is $\Delta t = T_b/10\,000$ for the simulations of fluid flow and plate deformation. Besides, a finite moving computational domain [21] is used in the x direction to allow the plate to move for a sufficiently long time. As the plate travels one lattice in the x direction, the computational domain is shifted; i.e., one layer is added at the inlet and another layer is removed at the outlet [21].

Figure 2 shows the streamwise velocity of the leading edge as a function of time. It is seen that the present result is consistent with that of Ref. [16]. The results of grid independence and time step independence are shown in Fig. 3. It is seen that $\Delta x/L = 0.01$ and $\Delta t/T_b = 0.0001$ are sufficient to achieve accurate results. Therefore, $\Delta x/L =$
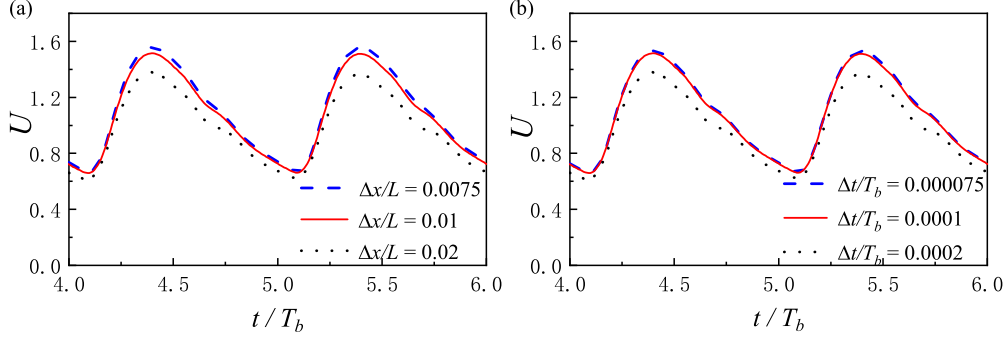
FIG. 3. The grid independence (a) and time step independence (b) studies for the HT mode with $K = 1$ and DC $= 0.5$. The cruising speed U as a function of time is presented, and $T_b = 1/f_0$ is the burst period.

0.01 and $\Delta t/T_b = 0.0001$ were adopted in all of the present simulations.

Besides, the numerical strategy used in this study has been validated and successfully applied to a wide range of flows, such as the coupling performance of tandem flexible inverted flags in a uniform flow [30] and the effect of the trailing-edge shape on the self-propulsive performance of heaving flexible plates [32].

IV. RESULTS AND DISCUSSION

All key parameters in this study are shown in Table I. Among them, four parameters are fixed: Re, A, M, and S, which are identical to those in Refs. [16,18,19]. While other parameters are variable: the bending stiffness K, the duty cycle DC, and the frequency ratio f_r. In addition, the stretching stiffness (S) is equal to 1000, which is large enough so that the stretching deformation is negligible. It is noted that the case with DC $= 1$ for intermittent swimming (including the MT and HT modes) and the case with $f_r = 1$ for the CT mode are identical.

A. Performances of the three swimming modes

First, three typical cases with identical rigidity ($K = 1$) but different swimming modes are tested. In the cases of the MT and HT modes, the typical DC is set to be 0.5. In the CT mode $f_r = 1$. Typical instantaneous cruising speeds as functions of time in the three cases with $K = 1$ are shown in Fig. 4. Among the three cases, it is seen that the mean cruising speed U of the CT mode is higher than those of the intermittent swimming modes. U of the HT mode seems a little bit higher than that of the MT mode, although it has the same value of DC. The Re of the CT mode based on the cruising speed is about 350.

TABLE I. The key parameters in the simulations.

Reynolds number	Re	200
Heaving amplitude	A	0.5
Mass ratio	M	0.2
Stretching stiffness	S	1000
Bending stiffness	K	0.1, 1, 10
Duty cycle	DC	0.1, 0.2, 0.3, 0.4, 0.5, 0.6, 0.7, 0.8, 0.9, 1
Frequency ratio	f_r	0.3, 0.4, 0.5, 0.6, 0.7, 0.8, 0.85, 0.9, 0.95

From the zoom-in view [Fig. 4(b)] we can see that, in the CT mode, $u(t)$ is a sinusoidal function with two surging oscillations of about the average speed in one period, which has been observed in many previous self-propelled studies [9,17]. For the HT mode, the pattern of $u(t)$ sharpens near peaks and turns into the sawtooth-shaped wave form [12]. For the MT mode, there are two successive peaks during the burst period. When it comes to the coast period, the speed drops rapidly and nonlinearly due to the drag force.

To further evaluate the performance of the swimming, the cost of transport (COT), the mean swimming power P_{ave}, the input work W, and the efficiency η are introduced. The COT is a useful performance metric, which is widely used in biology. The physical meaning of the COT is the amount of energy that it takes to swim a unit distance. The COT is reported on a per unit mass basis and has the dimension of acceleration. Hence, generally speaking, a swimmer with the smaller value of the COT is preferred. Specifically, it is defined as

$$\mathrm{COT} = \frac{P_{\mathrm{ave}}}{mU}, \tag{11}$$

where m is the mass of the swimmer and U is the mean cruising speed. P_{ave} and U are defined as

$$P = \int_0^1 F \cdot \frac{\partial X}{\partial t} ds, \qquad P_{\mathrm{ave}} = \frac{1}{T_{\mathrm{cyc}}} \int_{t'}^{t'+T_{\mathrm{cyc}}} a(t)P dt, \tag{12}$$

$$U = -\frac{1}{T_{\mathrm{cyc}}} \int_{t'}^{t'+T_{\mathrm{cyc}}} \left(\frac{\partial X}{\partial t} \bigg|_{s=0} \right) dt, \tag{13}$$

where P is the instantaneous power, F represents the force on the surrounding fluid by the plate, and $a(t)$ is the shielding function [12], i.e.,

$$a(t) = \begin{cases} 1, & \text{if } t \in \text{ active burst period,} \\ 0, & \text{otherwise.} \end{cases} \tag{14}$$

It is noted that, for the CT mode, $T_{\mathrm{cyc}} = \frac{T_b}{f_r}$, with $f_r \leqslant 1$. U in the case with $f_r = 1$ may be the largest. In the following, COT and U are normalized by the corresponding quantities in the CT mode with $f_r = 1$ [12], i.e.,

$$\mathrm{COT}^* = \frac{\mathrm{COT}}{\mathrm{COT}|_{f_r=1}}, \tag{15}$$
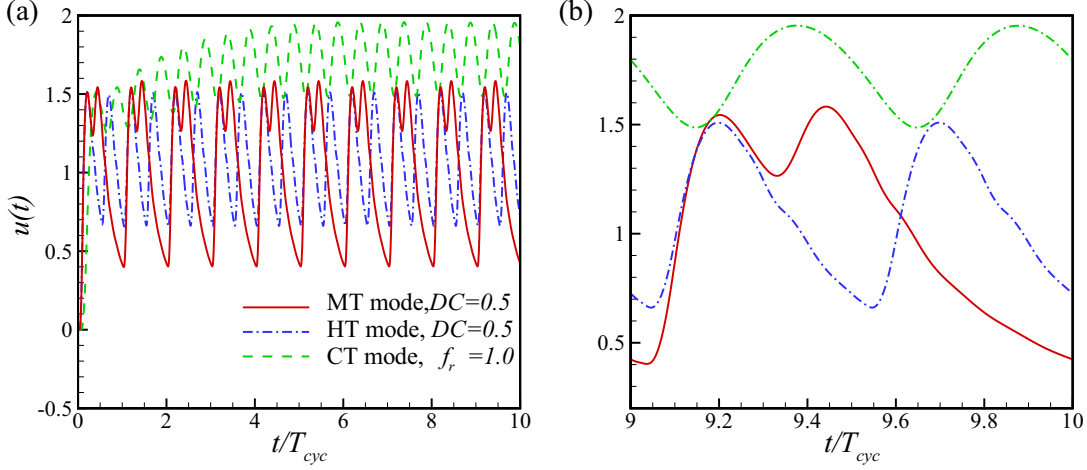
$$U^* = \frac{U}{U|_{f_r=1}}. \tag{16}$$

FIG. 4. (a) The instantaneous cruising speeds of the plate as functions of time ($K = 1$). In the intermittent modes (the MT and HT modes), DC $= 0.5$, while in the CT mode, $f_r = 1$. (b) The zoom-in view of the speed within one period.

Second, we would like to discuss the performances of the three swimming modes, under the circumstances of different bending rigidity. Figure 5 shows the normalized cost of transport (COT*) as a function of U^* for $K = 0.1, 1$, and 10. It can be seen that the results are very different. For small K, i.e., $K = 0.1$ [Fig. 5(a)], the CT mode has the best performance in general because the COT* of the CT mode is smaller than that of the other two modes at the same U^* when $U^* < 0.9$. Meanwhile, the performance of the MT mode is not as good as that of the HT mode. It is noted that for the MT and HT modes, the maximum U arises at DC $= 0.9$ instead of at DC $= 1$ [see the points A and B in Fig. 5(a)], which is similar to the results of Ryu and Sung [15]. The reason may be that the presence of the short coast period can avoid a strong tension in the flexible plate in the longitudinal direction so that the flapping motions of the flexible plate are enhanced for DC $= 0.9$ [15].

Figure 5(b) shows the results of moderate K ($K = 1$). It is seen that the performance of the HT mode is the best because the COT* of the HT mode is the lowest. Besides, the MT mode also outperforms the CT mode for DC > 0.3. In other words, generally speaking, the intermittent swimming modes perform better than the CT mode at moderate K. The largest discrepancy of the COT between the HT and CT modes arises at DC ≈ 0.4 with an energy saving of 22% approximately, while that between the MT and CT modes arises at DC ≈ 0.6 with an energy saving of 9% approximately.

At a large K, i.e., $K = 10$, as shown in Fig. 5(c), the COT* of the HT mode is completely larger than that of the CT mode at any U^*. Besides, the COT* of the MT and CT modes are almost the same when DC $\geqslant 0.5$. When DC < 0.5, the COT* of the MT mode is larger than that of the CT mode. Hence, the intermittent swimming modes have no obvious advantage over the CT mode at large K.

Third, we would like to directly compare the two intermittent swimming modes. The mean cruising speed U, the input work W, and the propulsive efficiency η are further used to quantify the propulsive performance of the plate [16,19]. The input work W during one period is

$$W = P_{\text{ave}} T_{\text{cyc}}. \qquad (17)$$

The propulsive efficiency η is the ratio of the kinetic energy of the plate and the input work, i.e.,

$$\eta = \tfrac{1}{2} m U^2 / W. \qquad (18)$$

The results for the MT and HT modes are shown in Fig. 6. It is seen from Fig. 6(a) that the cruising speeds in cases of $K = 0.1$ are close to those of $K = 10$. Besides, U of $K = 1$ is significantly higher than U of $K = 0.1$ and 10. Figure 6(b) shows that the input works of $K = 1$ are slightly higher than those of $K = 10$, and the input works of $K = 0.1$ are significantly lower than those of $K = 1$ and 10. From the performances of the cases of $K = 1$, it seems the higher cruising speed is due to the larger input work. However, for the rigid cases ($K = 10$), the input work is large, but the cruising speed is low. Therefore, it is expected that the efficiency would be low for the cases of $K = 10$. The propulsive efficiency as a function of DC is shown in Figure 6(c). It is confirmed that η of the cases $K = 10$ is the lowest among the cases with different rigidities.

From Figs. 6(a) and 6(c), we can see that the open squares (the HT mode) are generally above the triangles (the MT mode) at cases of $K = 0.1$ and 1. Hence, in terms of the cruising speed and efficiency, the propulsive performance of the HT mode is better than that of the MT mode at $K = 0.1$ and 1. It is also seen that the situation is the opposite at $K = 10$; i.e., the MT is better. These results are consistent with the results of COT (Fig. 5). It is conjectured that the MT mode is not preferable at moderate and small K because it generates an asymmetric time-averaged velocity field and leads to nonzero averaged lateral forces [12]. The details are discussed in Sec. IV C.

B. Forces and powers

In the following, we try to reveal the propulsion mechanism through contributions of the forces exerted on the plate. Here three typical cases are analyzed. The key parameters of the three cases are shown in Table II. It is noted that the three cases achieve almost an identical cruising speed, which is $U^* \approx 0.58$ [see points C, D, and E in Fig. 5(b)].
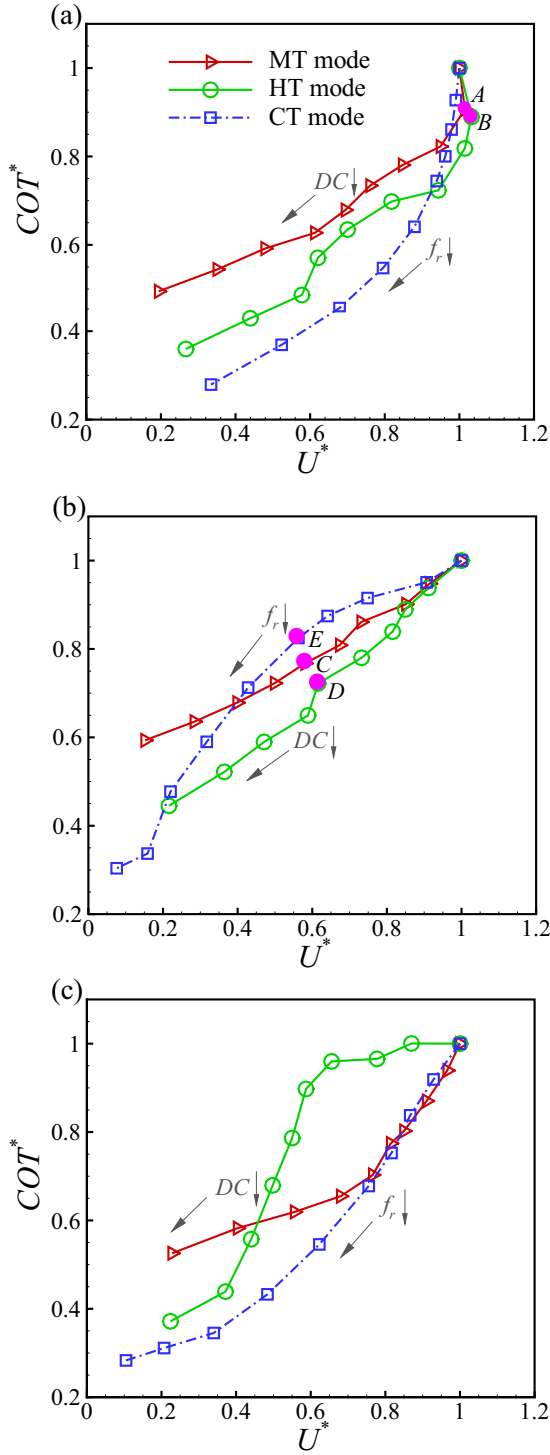
FIG. 5. The normalized cost of transport (COT*) as a function of the normalized mean cruising speed (U^*) for (a) $K = 0.1$, (b) $K = 1$, and (c) $K = 10$, respectively.
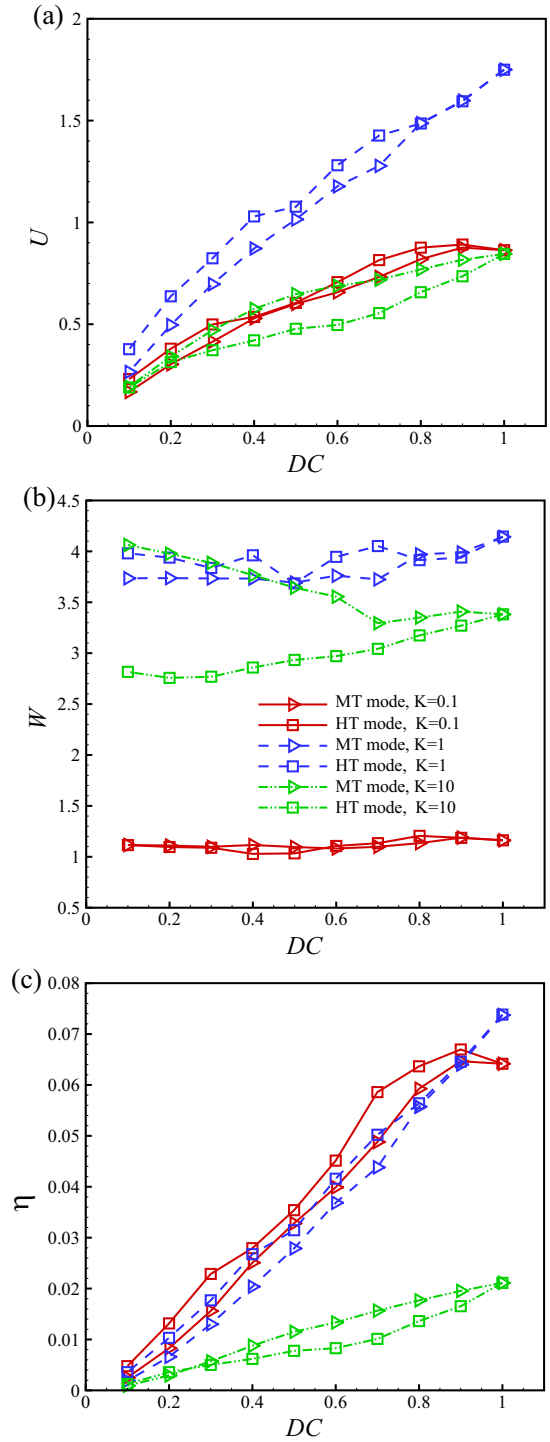

FIG. 6. Propulsive speed U (a), input work W (b), and propulsive efficiency η (c) as functions of DC for the MT and HT modes with $K = 0.1$, 1, and 10.

TABLE II. Key parameters in cases M, H, and C.

Case	Mode	Bending stiffness K	DC or f_r
Case M [C in Fig. 5(b)]	MT mode	1	DC = 0.5
Case H [D in Fig. 5(b)]	HT mode	1	DC = 0.5
Case C [E in Fig. 5(b)]	CT mode	1	$f_r = 0.8$

The Lagrangian force F_s, exerted on the plate by the surrounding fluid, can be decomposed into two parts: one is the normal force F^n, in which the pressure component dominates, and the other is the tangential force F^τ, which mainly comes from the viscous effects. These forces at the ith Lagrangian
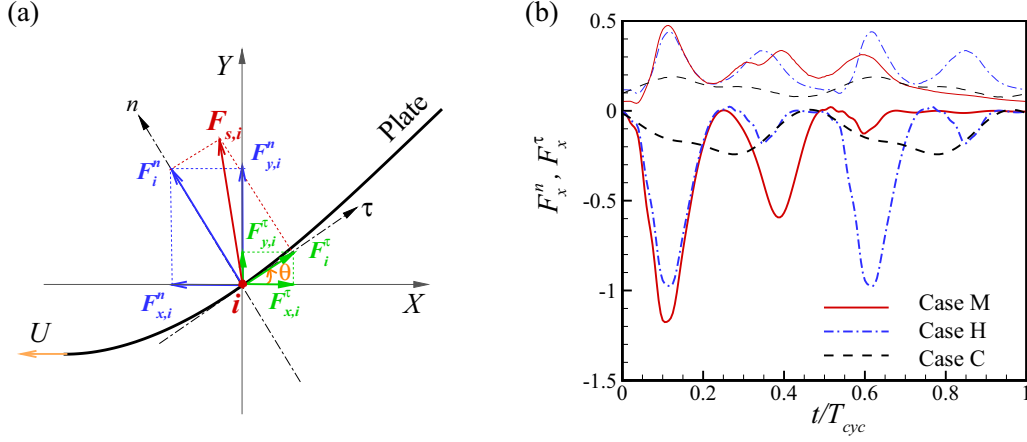
(a)

(b)

FIG. 7. (a) Schematic diagram for force decomposition. The black curved line represents the plate. The red dot represents the ith Lagrangian node. $\boldsymbol{\tau}$ and $\boldsymbol{n}$ denote the local tangential and normal vectors, respectively. θ is the angle between $\boldsymbol{\tau}$ and the positive direction of the x axis. The local slope is calculated by $\tan\theta$. (b) The total x-component of F^n and F^τ (i.e., $F_x^n = \sum_i F_{x,i}^n$ and $F_x^\tau = \sum_i F_{x,i}^\tau$) for the three cases as functions of time within one cycle period. Thick and thin lines represent F_x^n and F_x^τ, respectively. The forces are normalized by $F_{\text{ref}} = \frac{1}{2}\rho U_{\text{ref}}^2 L$.

node are defined as follows [19]:

$$F_{s,i} = [-p\boldsymbol{I} + \boldsymbol{T}] \cdot \boldsymbol{n} = F_i^n + F_i^\tau, \tag{19}$$

$$F_i^n = (F_{s,i} \cdot \boldsymbol{n})\boldsymbol{n} = \left(F_{x,i}^n, F_{y,i}^n\right), \tag{20}$$

$$F_i^\tau = (F_{s,i} \cdot \boldsymbol{\tau})\boldsymbol{\tau} = \left(F_{x,i}^\tau, F_{y,i}^\tau\right), \tag{21}$$

where $\boldsymbol{I}$ is the unit tensor, $\boldsymbol{T}$ is the viscous stress tensor, $\boldsymbol{\tau}$ is the unit tangential vector toward the trailing edge, $\boldsymbol{n}$ is the unit normal vector as shown in Fig. 7(a) in the schematic diagram, and [·] denotes the jump in a quantity across the immersed boundary. The power P_i can also be decomposed into two parts: P_i^n and P_i^τ, which are contributed by F_i^n and F_i^τ, respectively, i.e.,

$$P_i = F_{s,i} \cdot u = P_i^n + P_i^\tau, \tag{22}$$

$$P_i^n = F_i^n \cdot u = P_{x,i}^n + P_{y,i}^n, \tag{23}$$

$$P_i^\tau = F_i^\tau \cdot u = P_{x,i}^\tau + P_{y,i}^\tau, \tag{24}$$

where $P_{x,i}^n = F_{x,i}^n u$, $P_{y,i}^n = F_{y,i}^n v$, $P_{x,i}^\tau = F_{x,i}^\tau u$, and $P_{y,i}^\tau = F_{y,i}^\tau v$.

Figure 7(b) shows the total x-component of F^n and F^τ (i.e., $F_x^n = \sum_i F_{x,i}^n$ and $F_x^\tau = \sum_i F_{x,i}^\tau$) along the whole plate for the three cases as functions of time. It seems that F_x^n contributes much to a thrust because $F_x^n < 0$, while F_x^τ contributes to a drag since $F_x^\tau > 0$ within one cycle period. It is also noted that the time average of the total force in the x direction ($F_x^n + F_x^\tau$) is zero for all cases. The time averages of $|F_x^n|$ for cases M, H, and C are 0.194, 0.224, and 0.129, respectively. So, U^* values of the cases are 0.58, 0.60, and 0.56, respectively [see Fig. 5(b) or 6(a)].

The generation and distribution of F_x^n are mainly induced by the bending deformation of the flexible plate [19], which can be quantitatively described by the local slope. Figure 8 shows the time-averaged absolute local slope and the time-averaged F_x^n along the flexible plate for the three cases. It is seen that, compared to the MT mode, the bending deformation for the HT mode is larger, which would lead to a larger thrust F_x^n. Although the bending deformation of the CT mode is
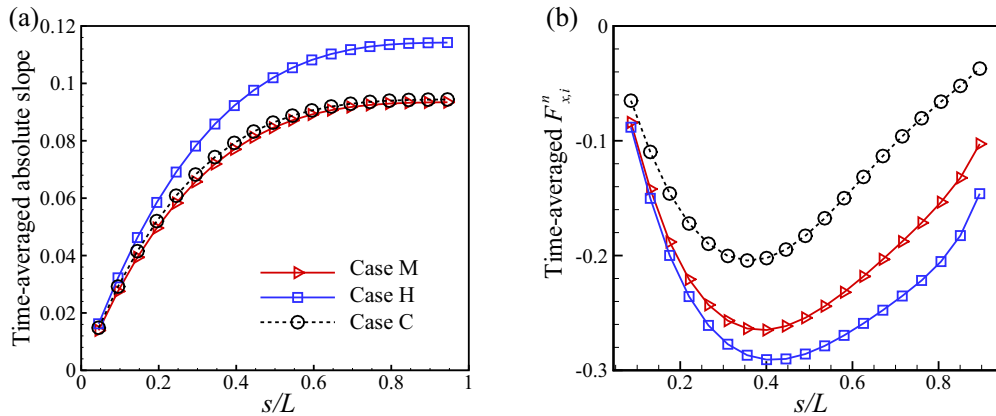
(a)

(b)

FIG. 8. (a) Time-averaged absolute local slope and (b) time-averaged $F_{x,i}^n$ along the flexible plate for the three cases. The forces are normalized by $F_{\text{ref}} = \frac{1}{2}\rho U_{\text{ref}}^2 L$.
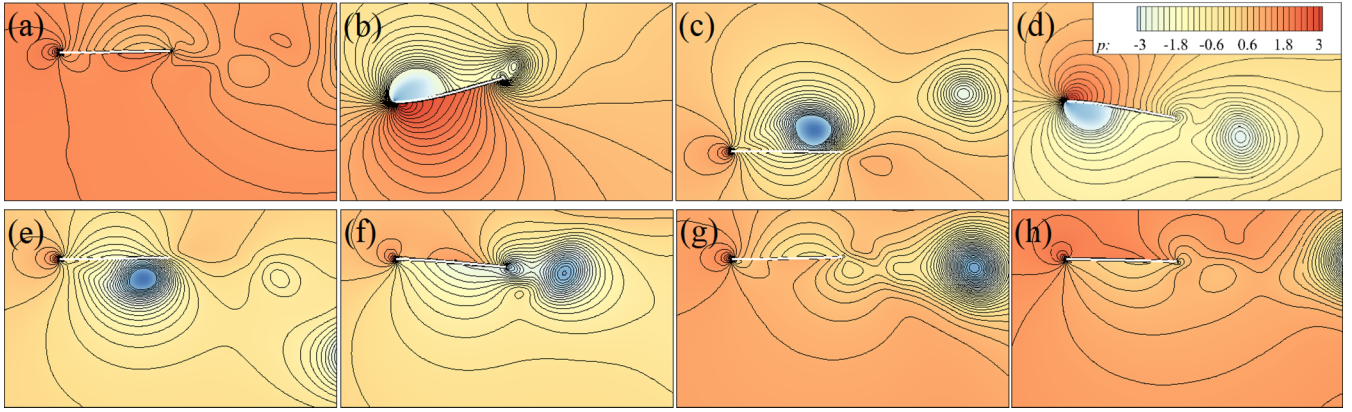
FIG. 9. Instantaneous pressure contours for case M (the MT mode, DC = 0.5, $K = 1$). The time interval between two adjacent contours is $T_{cyc}/8$.

close to that of the MT mode, the thrust F_x^n of the former is significantly smaller than that of the latter. Hence, the intermittent swimming styles do enhance the thrust.

$P_{x,i}^n$ is the power produced by $F_{x,i}^n$ (Eq. 23). Integrating $P_{x,i}^n$ with time along the whole plate within one period, we can obtain the values of the useful work done by F_x^n in cases M, H, and C, which are 0.707, 0.789, and 0.249, respectively. The corresponding total works are 3.890, 3.985, and 2.406, respectively. The corresponding ratios of the useful and total works are approximately 0.18, 0.20, and 0.10, respectively. Hence, the HT mode achieves the lowest COT [Fig. 5(b)] and the highest propulsive efficiency [Fig. 6(c)]. In other words, at moderate K, the performance of the HT mode is the best.

C. Flow structure

The propulsive behaviors of the flapping flexible plate are closely associated with the flow structure; thus, the pressure distribution and the vortical structures around the plate as well as the time-averaged streamwise velocity field are explored. First, the three cases in Table II are taken as examples to illustrate the influence of flow field on thrust and power. Figures 9–11 respectively show the instantaneous pressure contours of the three cases in one cycle period, and the time interval between two adjacent contours is $\frac{T_{cyc}}{8}$. It is seen that,

for the three cases, at $t = 0$, the pressure around the leading edge of the plate is higher and the deformation of the plate is small [Figs. 9(a)–11(a)]. At this time, the plate experiences net drag force. Figure 12(a) shows that $F_x > 0$ for the three cases when $t = 0$.

At $t = \frac{T_{cyc}}{8}$, the pressure on the upper surface is low while it is high on the lower surface [Figs. 9(b)–11(b)]. For cases M and H, due to the large bending deformation of the plate, the pressure difference leads to the thrust, i.e., $F_x < 0$ [see Fig. 12(a)]. However, for case C, the bending deformation and the pressure difference are both small, thus $F_x \approx 0$ [see Fig. 12(a)]. At $t = \frac{2T_{cyc}}{8}$, for cases M and H, because of the small bending deformation of the plate and the high pressure in the leading edge of the plate [Figs. 9(c) and 10(c)], the plate experiences a drag force [Fig. 12(a)]. While for case C, since the increase of the deformation and the pressure difference [Fig. 11(c)], the horizontal force for the plate is the thrust force, as shown in Fig. 12(a).

At $t = \frac{3T_{cyc}}{8}$, Fig. 9(d) shows that the deformation of the plate and the pressure difference across the plate are both large for case M, which leads to the thrust force [see Fig. 12(a)]. For case H, it is noted that the plate is experiencing that the coast period, the deformation, and the pressure difference are very small [see Fig 10(d)], thus the horizontal force for the plate is the drag force [see Fig. 12(a)]. As for case C, the deformation
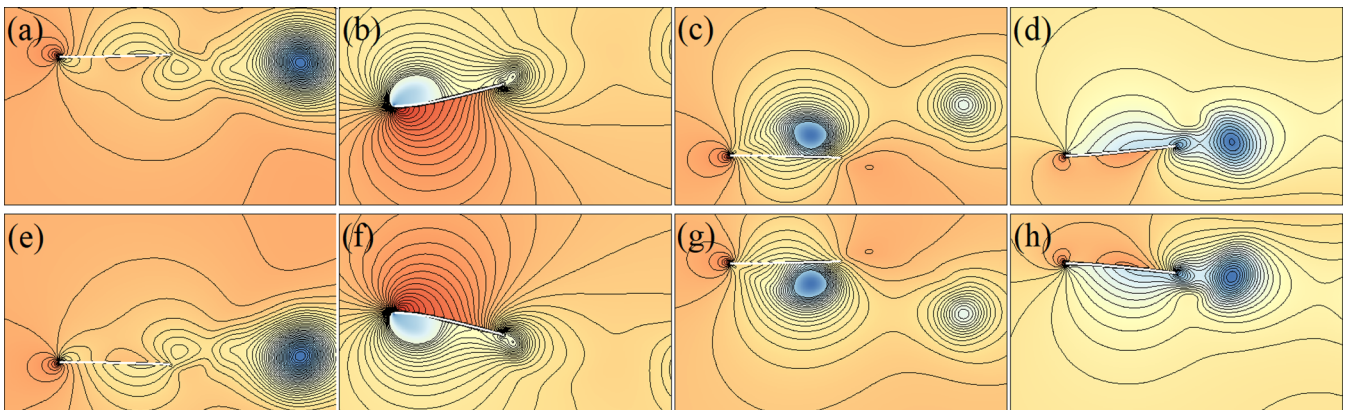

FIG. 10. Instantaneous pressure contours for case H (the HT mode, DC = 0.5, $K = 1$). The time interval between two adjacent contours is $T_{cyc}/8$. The contours are identical to those in Fig. 9.
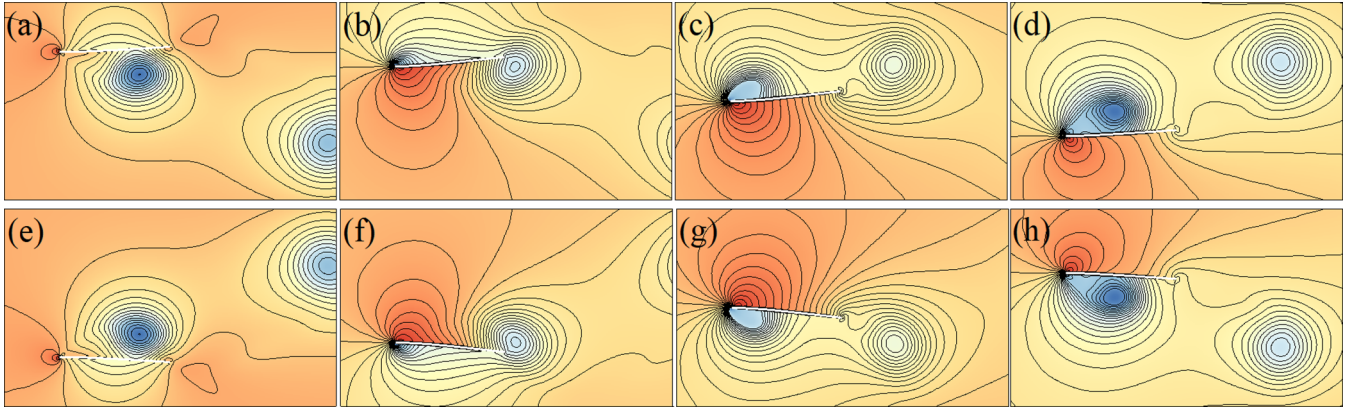
FIG. 11. Instantaneous pressure contours for case C (the CT mode, $f_r = 0.8$, $K = 1$). The time interval between two adjacent contours is $T_{cyc}/8$. The contours are identical to those in Fig. 9.

and the pressure difference are also small [see Fig. 11(d)], which leads to $F_x \approx 0$ [Fig. 12(a)].

When $t \geqslant \frac{4T_{cyc}}{8}$, the plate is in the coast period for case M, so it is predictable that the plate experiences net drag force [Fig. 12(a)], which also can be seen from Figs. 9(e)–9(h). For cases H and C, the pressure distribution and deformation of the plate look symmetric with respect to those at $t < \frac{4T_{cyc}}{8}$ (Figs. 10 and 11), which results in the same F_x as that in the first half period [Fig. 12(a)].

As can be seen from the above analysis and Fig. 12(a), the plate experiences net drag force in the coast period for intermittent modes, during the period the speed of the plate decreases dramatically (see Fig. 4, the instantaneous speed reduces 70% and 50% in the MT and HT modes, respectively). Hence, despite the speed increases during the burst period, the overall cruising speed in the intermittent modes may be similar to that in the CT mode.

Figure 12(b) shows the time history of power for the three cases. For the intermittent modes (cases M and H), there are two peaks during the burst phase, corresponding to the down-stroke and the up-stroke respectively, similar to those in the continuous mode (case C). It can be seen that, for the intermittent modes, although the power is high during the burst phase, it is almost zero during the coast phase. In other

words, the intermittent swimmers save the input power during the coast phase. In this way, the average power (or the COT) of the intermittent mode may be lower than that of the CT mode within one cycle.

The vortex shedding behind the plate for various swimming modes and bending stiffness are compared in Fig. 13. Here the results with DC $= 0.5$ for the intermittent modes and $f_r = 0.8$ for the CT mode are presented. The results of $K = 0.1$ are very similar to those of $K = 1$ and they are not shown here. Results indicate that four vortices are shed from the tail of the plate within one period for both intermittent modes, but the vortex streets behind the plate are very different.

For the MT mode, when K is moderate, i.e., $K = 1$ [Fig. 13(a)], two strong vortices (A and B1) form a strong vortex dipole, while a weaker vortex B2 and a strong vortex C form a pair. The vortex B2, which decays rapidly, generates from the broken effect of B1. There is a much smaller and weaker vortex D shedding from the tail finally, which dissipates quickly. Thus, only vortices A, B1, B2, and C are visible in the downstream. The vortex dipole and the "weak-strong" vortex pair travel along two straight lines which compose two vortex streets. When K is large, i.e., $K = 10$, the results are similar to those of $K = 1$, but the vortices become chaotic
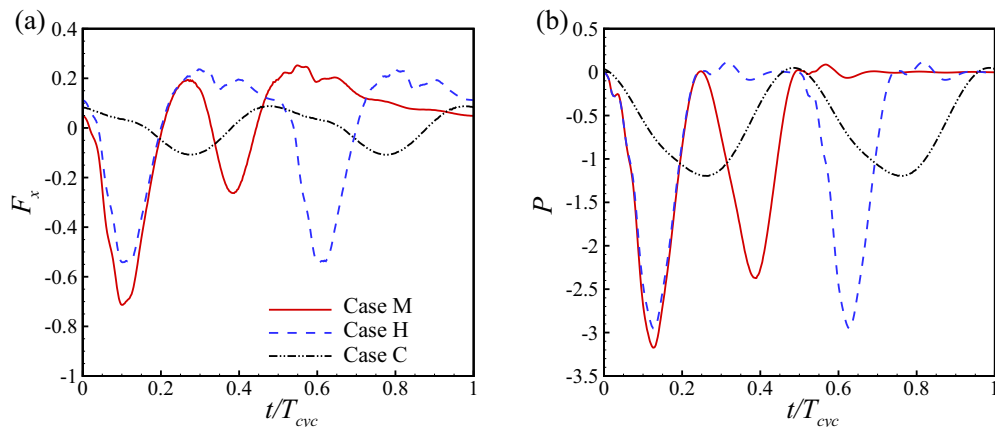

FIG. 12. Horizontal force experienced by the plate (a) and the power of the plates (b) as functions of time in one period for cases M, H, and C. The forces and powers are normalized by $F_{ref} = \frac{1}{2}\rho U_{ref}^2 L$ and $P_{ref} = \rho U_{ref}^3 L$.
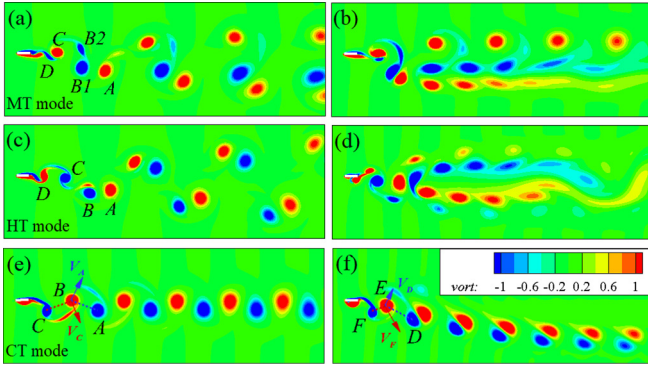
FIG. 13. Vorticity contours for three swimming modes. The left and right columns are cases of $K = 1$ and $K = 10$, respectively. From top to bottom, the rows are the cases of the MT (DC = 0.5), HT (DC = 0.5), and CT ($f_r = 0.8$) modes, respectively. A, B, C, D, E, F, B1, and B2 are the marks of vortices.
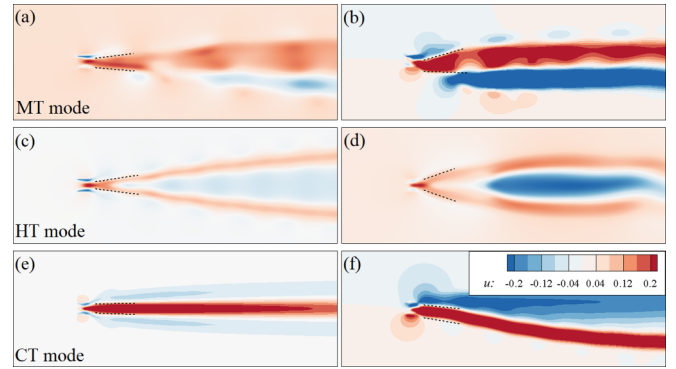

FIG. 14. Time-averaged streamwise velocity field for the three swimming modes. The left and right columns are cases of $K = 1$ and $K = 10$, respectively. From top to bottom, the rows are the cases of the MT (DC = 0.5), HT (DC = 0.5), and CT ($f_r = 0.8$) modes, respectively.

in the downstream [Fig. 13(b)]. In the MT mode, the motion itself is asymmetric [see Fig. 1(a)], and it is not surprising that an asymmetric flow field occurs [9].

For the HT mode, when $K = 1$ [Fig. 13(c)], four vortices [see vortices A, B, C, and D in Fig. 13(c)] form two strong vortex dipoles, which travel along two straight lines and compose two identical vortex streets. That is consistent with the result in the experiments about the HT-mode swimming of koi carps [11]. But when $K = 10$, the vortices become chaotic in the downstream [Fig. 13(d)]. The situation is similar to that in the MT mode. It is noted that the vorticity dissipation is significant in Figs. 13(b) and 13(d), and the vortex streets cannot keep their structures up to a long distance in the wake.

For the CT mode, there is a classic reverse Karman vortex street in the wake when $K = 1$ [Fig. 13(e)]. However, for the large K, the wake deflects downwards [Fig. 13(f)], which is referred to as "the symmetry breaking" [17,33–35]. Hence, it seems that the foil flexibility is helpful to preserve the symmetry of the reverse Karman vortex street, which is consistent with the results of Marais *et al.* [34] and Zhu *et al.* [17].

Here, we give a brief explanation in terms of vortex-induced velocity. As shown in Fig. 13(e), the movement of vortex B is mainly determined by the nearby vortices (A and C). Vortices A and C that have identical strength look almost symmetric about vortex B. So the induced velocities V_A and V_C are symmetric up and down, and the velocity of vortex B $V_B = V_A + V_C$ is horizontal. Hence, the vortex street does not deflect. While in Fig. 13(f), the induced velocities by vortices D and F, i.e., V_F and V_D are not symmetric. Thus, the movement of vortex E is deflected, so is the vortex street. Similar analysis is applicable to other cases in Fig. 13.

Figure 14 shows the time-averaged streamwise velocity field for different swimming modes and bending stiffness. The results of $K = 0.1$ are very similar to those of $K = 1$ and they are not shown here. It is seen that, for all three rigidity cases, the velocity field of the MT mode is always asymmetric [Figs. 14(a) and 14(b)], because the motion of the MT mode is asymmetric. However, the HT mode has a symmetric jet structure when K is small or moderate [Fig. 14(c)] but the jet becomes irregular and asymmetric at large K [Fig. 14(d)]. The

situation of the CT mode looks similar to that of the HT mode [Figs. 14(e) and 14(f)].

The symmetry of wake has a significant effect on propulsion performance. In the study of Marais *et al.* [34], the average thrust is up to three times greater for the flexible foil (symmetric wake) than for the rigid foil (asymmetric wake). Zhu *et al.* [17] showed that the propulsive efficiency of the cases with asymmetric wakes is much lower compared with the cases with symmetric wakes. As we know, the plate moves forward by pushing the fluid backward. In the HT mode, the wake is symmetric. The backward momentum of the fluid or the reverse Karman vortex, and therefore the generated thrust force, would be totally in the x direction. However, in the MT mode, because the wake is asymmetric, the backward momentum of the fluid would not fully be used to propel the plate forward. In other words, part of the backward momentum of the fluid is wasted in the lateral direction. Hence, the asymmetric time-averaged streamwise velocity field in the MT mode has a negative effect on the propulsive performance.

Generally speaking, the plate achieves a better propulsion performance when the jet inclination angle is smaller [19,36]. For example, in Fig. 14 the jet inclination angle of the left column ($K = 1$) is smaller than that of the corresponding right column ($K = 10$), so the thrust and cruising speed are larger in the cases of $K = 1$ (see Fig. 6).

However, the connection between jet structure and propulsion performance is only applicable to the cases of the same swimming mode, which has identical vortex shedding patterns. When vortex shedding patterns are different, the connection may be not applicable. For example, in the HT mode, there are two vortex streets in the wake, while in the CT mode there is a single vortex street. Two vortex streets generally have a larger jet inclination angle. Nevertheless, it does not necessarily mean that the case with two vortex streets must have a smaller thrust force than that of the single vortex street. It is also noticed that, in the studies of Dong *et al.* [36] and Peng *et al.* [19], the connection between jet structure and cruising speed is only applicable to the cases in which the flow structures (vortex shedding patterns) are similar.

V. CONCLUSIONS

The propulsive performances of intermittent and continuous swimming of a self-propelled flapping plate are investigated numerically. It is found that when K is moderate [i.e., $K \approx O(1)$] and the duty cycle is not too small, the intermittent swimming modes, including the HT and MT modes, are more economical than the CT mode. Besides, in terms of the mean speed U and propulsive efficiency η, the HT mode is better than the MT mode when K is small or moderate.

We analyze the bending deformation and decompose the forces and the power of the plate to explain the above results. Three cases with moderate K (Table II) are taken as examples. The results show that the bending deformation of the HT mode is the largest, which may result in the largest thrust. The useful work done by the thrust and the total work are calculated, it is found that the ratio of useful work and total work for the HT mode is the largest. Therefore, the HT mode achieves the highest propulsive efficiency and the lowest cost of transport among the three cases.

The flow fields of three swimming modes are explored. Results show that four vortices are shed from the tail of the plate within one total period in the cases of the HT and MT modes, while two vortices are shed per period in the case of the CT mode. It is found that at the moderate K, the time-averaged streamwise velocity of the MT mode is asymmetric, while that of the HT mode is symmetric. Since the symmetric wake is favorable to generate more thrust force, the performance of the HT mode is better than that of the MT mode.

In the study, the mass ratio M is fixed to be 0.2 and the result may be only applicable to the situation of fish fins. The present results may be helpful to further understand the intermittent locomotion of fish and may be useful for bionic design.

[1] A. C. Gleiss, S. J. Jorgensen, N. Liebsch, J. E. Sala, B. Norman, G. C. Hays, F. Q. E. Grundy, C. Campagna, A. W. Trites, B. A. Block, and R. P. Wilson, Convergent evolution in locomotory patterns of flying and swimming animals, Nat. Commun. **2**, 352 (2011).

[2] J. M. V. Rayner, P. W. Viscardi, S. Ward, and J. R. Speakman, Aerodynamics and energetics of intermittent flight in birds, Am. Zool. **41**, 188 (2001).

[3] B. W. Tobalske, Morphology, velocity, and intermittent flight in birds, Am. Zool. **41**, 177 (2001).

[4] R. Kawabe, Y. Naito, K. Sato, K. Miyashita, and N. Yamashita, Direct measurement of the swimming speed, tailbeat, and body angle of Japanese flounder (*Paralichthys olivaceus*), ICES J. Mar. Sci. **61**, 1080 (2004).

[5] T. M. Williams, Intermittent swimming by mammals: A strategy for increasing energetic effciency during diving, Am. Zool. **41**, 166 (2001).

[6] D. Weihs, Energetic advantages of burst swimming of fish, J. Theor. Biol. **48**, 215 (1974).

[7] D. Weihs, Energetic significance of changes in swimming modes during growth of larval anchovy Engraulis mordax, Fishery Bull. **77**, 597 (1980).

[8] M. J. Lighthill, Large-amplitude elongated-body theory of fish locomotion, Proc. R. Soc. London, Ser. B **179**, 125 (1971).

[9] E. Akoz and K. W. Moored, Unsteady propulsion by an intermittent swimming gait, J. Fluid Mech. **834**, 149 (2018).

[10] G. Ribak, D. Weihs, and Z. Arad, Submerged swimming of the great cormorant *Phalacrocorax carbo sinensis* is a variant of the burst-and-glide gait, J. Exp. Biol. **208**, 3835 (2005).

[11] G. Wu, Y. Yang, and L. Zeng, Kinematics, hydrodynamics and energetic advantages of burst-and-coast swimming of koi carps (*Cyprinus carpio koi*), J. Exp. Biol. **210**, 2181 (2007).

[12] L. Dai, G. He, X. Zhang, and X. Zhang, Intermittent locomotion of a fish-like swimmer driven by passive elastic mechanism, Bioinspir. Biomim. **13**, 056011 (2018).

[13] G. V. Lauder, Fish locomotion: Recent advances and new directions, Annu. Rev. Mar. Sci. **7**, 521 (2015).

[14] M.-H. Chung, On burst-and-coast swimming performance in fish-like locomotion, Bioinspir. Biomim. **4**, 036001 (2009).

[15] J. Ryu and H. J. Sung, Intermittent locomotion of a self-propelled plate, Phys. Fluids **31**, 111902 (2019).

[16] X. Zhu, G. He, and X. Zhang, Flow-Mediated Interactions between Two Self-Propelled Flapping Filaments in Tandem Configuration, Phys. Rev. Lett. **113**, 238105 (2014).

[17] X. Zhu, G. He, and X. Zhang, How flexibility affects the wake symmetry properties of a self-propelled plunging foil, J. Fluid Mech. **751**, 164 (2014).

[18] Z.-R. Peng, H. Huang, and X.-Y. Lu, Hydrodynamic schooling of multiple self-propelled flapping plates, J. Fluid Mech. **853**, 587 (2018).

[19] Z.-R. Peng, H. Huang, and X.-Y. Lu, Collective locomotion of two closely spaced self-propelled flapping plates, J. Fluid Mech. **849**, 1068 (2018).

[20] B. S. H. Connell and D. K. P. Yue, Flapping dynamics of a flag in a uniform stream, J. Fluid Mech. **581**, 33 (2007).

[21] R.-N. Hua, L. Zhu, and X.-Y. Lu, Locomotion of a flapping flexible plate, Phys. Fluids **25**, 121901 (2019).

[22] C. S. Peskin, The immersed boundary method, Acta Numer. **11**, 479 (2002).

[23] R. Mittal and G. Iaccarino, Immersed boundary methods, Annu. Rev. Fluid Mech. **37**, 239 (2005).

[24] S. Y. Chen and G. D. Doolen, Lattice Boltzmann method for fluid flows, Annu. Rev. Fluid Mech. **30**, 329 (1998).

[25] Z. Guo, C. Zheng, and B. Shi, Discrete lattice effects on the forcing term in the lattice Boltzmann method, Phys. Rev. E **65**, 046308 (2002).

[26] C. Tang, H. Huang, P. Gao, and X.-Y. Lu, Self-propulsion of a flapping flexible plate near the ground, Phys. Rev. E **94**, 033113 (2016).

[27] W. Wang, H. Huang, and X.-Y. Lu, Self-propelled plate in wakes behind tandem cylinders, Phys. Rev. E **100**, 033114 (2019).

[28] J. F. Doyle, *Nonlinear Analysis of Thin-Walled Structures: Statics, Dynamics, and Stability* (Springer-Verlag, New York, 2001).

[29] F.-B. Tian, H. Luo, L. Zhu, and X.-Y. Lu, Interaction between a flexible filament and a downstream rigid body, Phys. Rev. E **82**, 026301 (2010).

[30] H. Huang, H. Wei, and X.-Y. Lu, Coupling performance of tandem flexible inverted flags in a uniform flow, J. Fluid Mech. **837**, 461 (2017).

[31] Q. Zou and X. He, On pressure and velocity boundary conditions for the lattice Boltzmann BGK model, Phys. Fluids **9**, 1591 (1997).

[32] C. Zhang, H. Huang, and X.-Y. Lu, Effect of trailing-edge shape on the self-propulsive performance of heaving flexible plates, J. Fluid Mech. **887**, A7 (2020).

[33] R. Godoy-Diana, C. Marais, J.-L. Aider, and J. E. Wesfreid, A model for the symmetry breaking of the reverse Benard–von Karman vortex street produced by a flapping foil, J. Fluid Mech. **622**, 23 (2009).

[34] C. Marais, B. Thiria, J. E. Wesfreid, and R. Godoy-Diana, Stabilizing effect of flexibility in the wake of a flapping foil, J. Fluid Mech. **710**, 659 (2012).

[35] R. Godoy-Diana, J.-L. Aider, and J. E. Wesfreid, Transitions in the wake of a flapping foil, Phys. Rev. E **77**, 016308 (2008).

[36] H. Dong, R. Mittal, and F. M. Najjar, Wake topology and hydrodynamic performance of low aspect-ratio flapping foils, J. Fluid Mech. **566**, 309 (2006).